

Dispersion of Solute by Electrokinetic Flow through Post Arrays and Wavy-Walled Channels

J. J. Kirchner and E. F. Hasselbrink, Jr.*

Department of Mechanical Engineering, University of Michigan, Ann Arbor, Michigan 48109-2125

In this work, we simulate electrokinetically driven transport of unretained solute bands in a variety of two-dimensional spatially periodic geometries (post arrays as well as sinuous/varicose channels), in the thin Debye layer limit. Potential flow fields are calculated using either an inverse method or a Schwarz–Christoffel transform, and transport is modeled using a Monte Carlo method in the transformed plane. In this way, spurious “numerical diffusion” transverse to streamlines is completely eliminated, and streamwise numerical diffusion is reduced to arbitrary precision. Late-time longitudinal dispersion coefficients are calculated for Peclet numbers from 0.1 to 3162. In most geometries, a Taylor–Aris-like scaling law for the dispersion coefficient $D_L/D_{L0} = 1 + Pe^2/\alpha$ underpredicts dispersion when $Pe \sim O(\alpha^{1/2})$ (here D_{L0} is the effective axial diffusion coefficient in the periodic geometry). A two-parameter correlation widely used in the porous media literature, $D_L/D_{L0} = 1 + Pe^n/\alpha$, agrees slightly better, but much better agreement can be obtained using a new quadratic form: $D_L/D_{L0} = 1 + Pe/\alpha_1 + Pe^2/\alpha_2$. A quasi-universal relationship for streamwise dispersion is offered that predicts 96% of the simulation data to within a factor of 2 in all geometries studied. Comparison with previous work shows that in circular post arrays, the dispersion coefficient for electrokinetic flow is a factor of 3–10 less (depending on Pe and relative post size) than for pressure-driven flow.

Post arrays are a recurring engineering motif in microscale analytical devices because they can be used as sieves, as geometric supports for very shallow channels (e.g., to prevent sagging during high-temperature bonding), or as solid supports for semisolid salt bridges or other polymer media. They are also attracting attention as engineered liquid chromatography media, due to the ease with which unprecedented geometric regularity can be achieved. He et al.¹, for example, used deep reactive ion etching to create post arrays of arbitrary geometry (Figure 1) and demonstrated that performance improvements are indeed possible when tight geometric control is exerted over the media.

The question “how much dispersion?” arises nowadays in discussions of the relative merits of capillary electrochromatog-

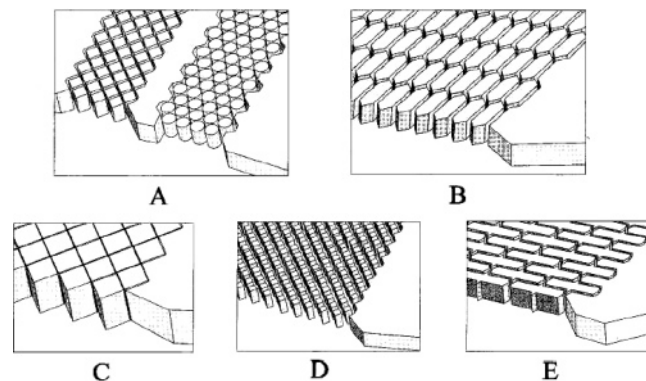


Figure 1. He et al.¹ concepts for microfabricated separations media.

raphy (CEC) versus high-performance liquid chromatography (HPLC). It is often argued that CEC has an advantage because ideal electrokinetic flow leads to reduced hydrodynamic dispersion compared with pressure-driven flow (as used in HPLC). This is certainly true in straight channels, because ideal electrokinetic flow through microchannels (uniform fluid and wall properties, dielectric walls, and vanishingly thin electric double layers (EDLs)) is purely potential^{5–7} and yields a flat velocity profile with no variation across the span of the channel. Indeed, there are data to support the assertion that the dispersion in packed columns is less for electrokinetic flow than for pressure-driven flow.⁸

On the other hand, it is also well known that U-turns, intersections, and similar channel geometries^{6,7,9} can create significant dispersion even with pure electrokinetic transport. Thus, one major goal of this paper is to conduct a relatively comprehensive study of the dispersion of unretained solute in pure electrokinetic flow through post arrays, to see under what conditions the dispersion is significant. We note that a comprehensive comparison of CEC and HPLC is beyond the scope of the present work, since we only consider unretained solutes. Common sources of band broadening include axial diffusion, hydrodynamic dispersion due to flow field gradients and cross-

- (2) Dutta, D.; Leighton D. T. *Anal. Chem.* **2002** *74*(5), 1007–1016.
- (3) Dutta, D.; Leighton D. T. *Anal. Chem.* **2003** *75*(1), 57–70.
- (4) Giddings, J. C. *J. Chromatogr.* **1961** *5*, 4–60.
- (5) Cummings, E. B.; Griffiths, S. K.; Nilson, R. H.; Paul, P. H. *Anal. Chem.* **2000**, *72*, 2526–2532.
- (6) Griffiths, S. K.; Nilson, R. H. *Anal. Chem.* **2000**, *72*, 5473–5482.
- (7) Griffiths, S. K.; Nilson, R. H. *Anal. Chem.* **2001**, *73*, 272–278.
- (8) Tallarek, U.; Rapp, E.; Scheenen, T.; Bayer, E.; Van As, H. *Anal. Chem.* **2000**, *72*, 2292–2301.
- (9) Culbertson, C. T.; Jacobson, S. C.; Ramsey, J. M. *Anal. Chem.* **1998**, *70*, 3781–3789.

* To whom correspondence should be addressed. E-mail: efhass@engin.umich.edu. Fax: (734) 647-7859.

(1) He, B.; Tait, N.; Regnier, F. *Anal. Chem.* **1998**, *70*, 3790–3797.

71 streamline mass transfer, and surface chemistry equilibrium, and
 72 in general, flow and chemical equilibrium are not separable as
 73 independent effects.²⁻⁴

74 Extensive previous work on dispersion of unretained solutes
 75 exists, but nearly all of it regards purely pressure-driven flow.
 76 Classical work by Taylor^{10,11} and Aris¹² shows that dispersion of
 77 solute in a round capillary convected by laminar pressure-driven
 78 flow behaves similarly to molecular axial diffusion, in that the band
 79 variance $\sigma^2 \propto D_L t$. Here D_L is the (longitudinal) dispersion
 80 coefficient, given by

$$D_L/D_{12} = 1 + Pe^2/\alpha \quad (1)$$

81 where D_{12} is the binary diffusion coefficient, the Peclet number
 82 $Pe = \bar{u}h/D_{12}$ is the ratio of convective influences to diffusive
 83 influences, \bar{u} is the mean velocity, and h is the capillary diameter.
 84 For a round capillary tube, Taylor and Aris found $\alpha = 192$; for
 85 pressure-driven flow between two plates, Wooding¹³ found $\alpha =$
 86 210 (defining h as the distance between the plates). Fried et al.¹⁴
 87 gave extensive discussion on both longitudinal and lateral disper-
 88 sions due to pressure-driven flow in porous media, and Adler¹⁵
 89 discussed asymptotic analysis of dispersion in porous media.
 90 Brenner¹⁶ developed a moment-based description of dispersion
 91 similar to that of Aris but for the more general flows found in
 92 spatially periodic porous media. Other workers¹⁷ have employed
 93 this method for various pressure-driven flows. Edwards and
 94 others^{18,19} presented data for dispersion in packed beds, also noting
 95 $D_L \propto Pe^n$ behavior with $n < 2$ for both experimental and numerical
 96 results. Kaviany²⁰ argued that a more general flow will have $D_L \propto$
 97 Pe^n dependence where $1 < n < 2$. Dutta and Leighton have
 98 quantified dispersion due to pressure-driven flow in wide channels
 99 of finite aspect ratio and have suggested novel channel shapes
 100 that minimize dispersion due to pressure-driven flow and gentle
 101 U-turns.^{2,3}

102 The problem for pure EOF and electrophoresis is simplified
 103 because electrophoretic and electroosmotic transport are potential
 104 flows if the product $\epsilon\zeta/\eta\sigma$ is uniform throughout the channel and
 105 the channel walls are an ideal dielectric material.⁵⁻⁷ In the present
 106 work, we simulate this type of electrokinetically driven geometric
 107 dispersion in several streamwise-periodic geometries using a
 108 Monte Carlo simulation for solute transport, with the benefit of a
 109 Schwartz-Christoffel transformation of the domain that makes a
 110 simpler and more accurate simulation possible. A powerful
 111 alternative would be Brenner's method¹⁶ for dispersion problems.
 112 However, this method only provides late-time behavior, and it is

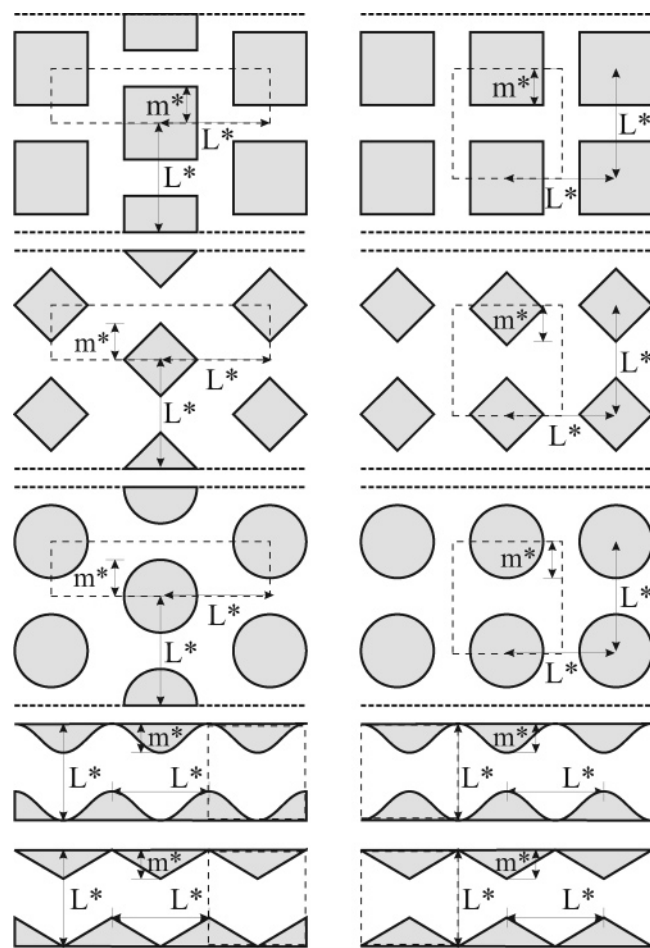


Figure 2. Geometries considered in the present work. The top three rows represent three geometries of infinitely periodic post arrays in staggered (left) and in-line (right) arrangements. The bottom two rows are the two wavy-walled channels considered in in-phase and out-of-phase geometries (phase referring to the phase of the periodic function defining the top and bottom walls). Dotted-line boxes in each case shows the periodic computational domain.

our intent to investigate early-time behavior in future work using
 the same code employed in the present work.

We consider a range of post array geometries typical of
 engineered chromatographic media: circular, diamond-shaped,
 and square posts at various fill ratios. We also consider wavy-
 walled channels, to approximate the effects of channel roughness
 and other lithography imperfections. We calculate effective
 longitudinal diffusion coefficients for a several periodic geometries
 over a wide range of Peclet number and correlate the results into
 a single “universal” dispersion function that collapses nearly all
 our data to within a factor of 2. It is hoped that the results can be
 useful as rules of thumb for the design and operation of columns
 incorporating post arrays, as well as a useful estimate of the effects
 of channel roughness on solute dispersion.

COMPUTATIONAL MODEL AND VALIDATION

Geometries. Figure 2 shows the three geometries of periodic
 post arrays (diamonds, circles, squares) and two geometries of
 wavy-walled channels (sinusoidal, sawtooth) in both arrangements
 (in-line, staggered) that are considered in the present work. The
 total of 10 different geometries are each parametrized by the

(10) Taylor, G. I. *Proc. R. Soc., London, Ser. A* **1953**, *219*, 186–203.
 (11) Taylor, G. I. *Proc. R. Soc., London, Ser. A* **1954**, *225*, 473–477.
 (12) Aris, R. *Proc. R. Soc., London, Ser. A* **1956**, *235*, 67–77.
 (13) Wooding, R. A. *J. Fluid Mech.* **1960**, *7*, 501–515.
 (14) Fried, J. J.; Combarous, M. A. *Advances in Hydrosience*; Academic: New York, 1971; Vol. 7.
 (15) Adler, P. M. *Porous Media: Geometry and Transports*; Butterworth-Heinemann: Stoneham, MA, 1992.
 (16) Brenner, H. *Philos. Trans. R. Soc. London, Ser. A* **1980**, *297*, 81–133.
 (17) Hoagland, D. A.; Prud'Homme, R. K. *AIChE J.* **1985**, *31*, 236–244.
 (18) Edwards, D. A.; Shapiro, M.; Brenner, M.; Shapira, M. *Transport Porous Media* **1991**, *6*, 337–358.
 (19) Eidsath, A.; Carbonell, R. G.; Whitaker, S.; Herrmann, L. R. *Chem. Eng. Sci.* **1983**, *38*, 1803–1816.
 (20) Kaviany, M. *Principles of Heat Transfer in Porous Media*, 2nd ed.; Springer: New York, 1995.

133 relative post size or wave amplitude m^* , which is the half-width
 134 of the square, radius of the circle, or half-diagonal of the diamond.
 135 The post spacing in the vertical and horizontal directions is L^* ;
 136 as shown in the figure, this is used to normalize m^* into a
 137 dimensionless parameter m defined as $m = m^*/L^*$. In this study,
 138 m was varied from 0.141 to 0.424 for diamonds, 0.150–0.395 for
 139 circles, and 0.1–0.35 for squares. For wavy channels, m was varied
 140 from 0.03 to 0.12. Note that, for in-line geometries, $m = 0.5$
 141 corresponds to complete channel blockage.

142 **Flow Solution.** In the thin Debye layer limit, the velocity of
 143 the i th species is $\mathbf{u}_i = (\mu_{EP,i} + \mu_{EO})\mathbf{E}$, where $\mu_{EP,i}$ and μ_{EO} are the
 144 electrophoretic and electroosmotic mobilities and \mathbf{E} is the electric
 145 field.^{5,21} Thus, the velocity field can be expressed as the gradient
 146 of a scalar potential, and the continuity and irrotationality of the
 147 field require that $\nabla_{xy}^2\phi(x, y) = 0$ and that $\nabla_{xy}^2\psi(x, y) = 0$, where
 148 the velocity potential ϕ and stream function ψ have impermeable
 149 wall boundary conditions at the channel walls. We normalize $\phi =$
 150 0 at $x = 0$ and $\phi = \Delta\phi$ at $x = 1$; ψ along the lower streamline is
 151 taken as zero, but ψ along the top streamline must be computed
 152 since it is equal to the flow rate through the system, which is not
 153 known a priori with a fixed potential gradient.

154 The most common way to solve for $\phi(x, y)$ and $\psi(x, y)$
 155 numerically is to approximate these equations by gridding the
 156 domain into finite differences or elements, but this requires higher-
 157 order methods or grid refinement to be accurate near sharp
 158 corners. An alternative approach is an inverse method (a special
 159 case of boundary-fitted coordinates), in which the problem is
 160 posed in (ϕ, ψ) -space, as described in previous references^{6,7,22,23}
 161 and in the Supporting Information. The domain is then a simple
 162 square, and boundary conditions and gridding become very easy
 163 to apply. This also has significant advantages in the scalar
 164 transport simulations, as will be evident momentarily. In this
 165 formulation the governing equations are

$$\nabla_{\phi\psi}^2\mathbf{x}(\phi, \psi) = \nabla_{\phi\psi}^2\mathbf{y}(\phi, \psi) = 0 \quad (2)$$

166 where the subscript $\phi\psi$ denotes derivatives in (ϕ, ψ) -space. These
 167 equations can be solved, using appropriate compatibility condi-
 168 tions, using second-order finite differences or by conformal
 169 mapping via the Schwarz–Christoffel transformation.^{24–30} Both
 170 were employed and compared, and although the methods agreed
 171 to within 1%, in general the latter proved to be much more robust.
 172 Since the Schwarz–Christoffel transformation is defined only for
 173 polygonal geometries, circles and sine waves were approximated
 174 by polygons made of 64 equal line segments, but squares and
 175 diamonds were defined exactly. Values of the x - and y -fields for a

regular grid of ϕ - and ψ -values were thus be found $x + iy =$ 176
 $f(\phi + i\psi)$ on a 601×601 grid. Solutions were validated by testing 177
 the orthogonality of x - and y -fields ($\nabla_{\phi\psi}\mathbf{x} \cdot \nabla_{\phi\psi}\mathbf{y} = 0$), which show 178
 relative error $O[10^{-3}]$, with most of the error occurring near 179
 regions where the boundary changes rapidly. Details are given 180
 in the Supporting Information available online. 181

Solute Transport. Finite element methods are particularly ill- 182
 suited to simulating scalar transport at high Peclet numbers. The 183
 natural formation of scalar gradients over very short length scales 184
 creates a computationally stiff problem subject to spurious 185
 “numerical diffusion”³¹ competing with the dispersive phenomena 186
 of interest. Since “apparent” diffusivity is the quantity we wish to 187
 compute, even modest numerical diffusion would be intolerable 188
 for this study. Therefore, the computational cost for typical finite 189
 differences/elements approaches would be quite high to achieve 190
 the needed accuracy. Using published rules of thumb for accurate 191
 simulation of convection–diffusion problems³² and Taylor’s crite- 192
 rion¹¹ for when dispersion reaches late-time behavior, the 193
 anticipated computational cost is $O[10Pe^{3.5}]$, which becomes very 194
 expensive at high Pe . 195

For these reasons we employ a Monte Carlo method,^{31–35} 196
 wherein the solute is represented by an ensemble of particles that 197
 undergo deterministic and random steps in space at each time 198
 step. This approach greatly diminishes many of the aforemen- 199
 tioned problems and has the advantage of lower computational 200
 cost $O[NPe^2]$, where N is the number of particles used to represent 201
 the solute. Additional advantages are obtained by following 202
 Griffiths and Nilson^{6,7} and conducting the simulation in (ϕ, ψ) - 203
 space. Each particle takes a deterministic step along a constant 204
 ψ -line corresponding to convection and a random step corre- 205
 sponding to diffusion. That is, defining our Peclet number as 206
 $Pe = (\Delta\phi/L^*)(L^*/D_{12})$ and setting $D_{12} = 1$ (without loss of 207
 generality), each particle takes a deterministic step proportional 208
 to $Pe\Delta t$ and a random step proportional to $(\Delta t)^{1/2}$. The random 209
 step’s length is also proportional to a normally distributed random 210
 number, and a split time stepping scheme is used for higher 211
 accuracy. More details of the time stepping and random step 212
 calculation methods, as well as code validation, are given in the 213
 Supporting Information. 214

Because the convection step is along constant ψ (a streamline), 215
 the method introduces no spurious transverse numerical diffusion 216
 even at infinite Pe . In addition to improved accuracy, the method 217
 reduces computational expense because we take full advantage 218
 of the periodicity of the domain by simply keeping track of which 219
 integer period each particle is in, and the use of the inverse 220
 domain also simplifies application of reflective boundary conditions 221
 for the particles, since the boundaries are square. The calculations 222
 are performed taking $\Delta\phi = 1$ and using varying values of D_{12} , 223
 but they could be performed equally well taking $D_{12} = 1$ and 224
 varying $\Delta\phi$, since it is only the dimensionless parameter Pe that 225
 matters. 226

(21) Santiago, J. G. *Anal. Chem.* **2001**, *73*, 2353–2365.
 (22) Jeppson, R. W. *J. Fluid Mech.* **1970**, *40*, 215–223.
 (23) Thom, A.; Apelt, C. J. *Field Computation in Engineering & Physics*; D. Van Nostrand: London, 1961.
 (24) Henrici, P. *Applied and Computational Complex Analysis*; John Wiley & Sons: New York, 1974.
 (25) Floryan, J. M. *J. Comput. Phys.* **1985**, *58*, 229–245.
 (26) Floryan, J. M.; Zemach, C. *J. Comput. Appl. Math.* **1993**, *46*, 77–102.
 (27) Batchelor, G. K. *An Introduction to Fluid Dynamics*; Cambridge University: New York, 2000.
 (28) Driscoll, T. A. *ACM T. Math. Software* **1996**, *22*, 168–186.
 (29) Driscoll, T. A.; Trefethen, L. N. *Schwarz-Christoffel Mapping*; Cambridge University: New York, 2002.
 (30) Driscoll, T. A. *Schwarz-Christoffel Toolbox for MATLAB*; <http://www.math.Udel.edu/~driscoll/software/SC/>, 2003.

(31) Fogelson, A. L. *J. Comput. Phys.* **1992**, *100*, 1–16.
 (32) Oran, E. S.; Boris, J. P. *Numerical Simulation of Reactive Flow*; Elsevier: New York, 1987.
 (33) Sherman, A. S.; Peskin, C. S. *SIAM J. Sci. Stat. Comput.* **1986**, *7*, 1360–1372.
 (34) Ghoniem, A. F.; Sherman, F. S. *J. Comput. Phys.* **1985**, *61*, 1–37.
 (35) Hammersley, J. M.; Handscomb, D. C. *Monte Carlo Methods*; Methuen: London, 1964.

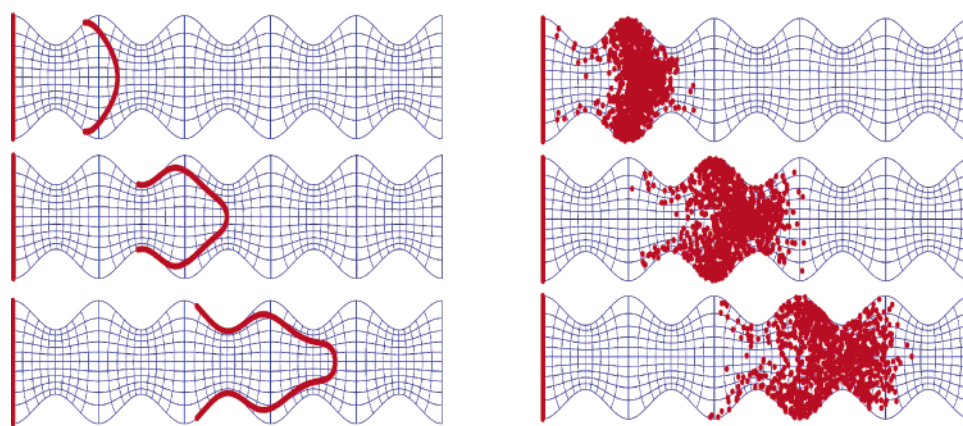


Figure 3. Early time series of Monte Carlo simulation of solute transport in sinusoidal wavy-walled channels ($m = 0.12$). Grid lines are streamlines and isopotential lines, and dots represent solute “particles”. The line at left in each frame shows the initial location of the particles at the start of the simulation. Left: three snapshots in time at $Pe = \infty$. The inverse/Monte Carlo simulation method tracks the solute band faithfully even at infinite Peclet number without spurious numerical diffusion; this would be virtually impossible using a finite differences/elements approach. Right: Early time series for the same geometry at $Pe = 100$.

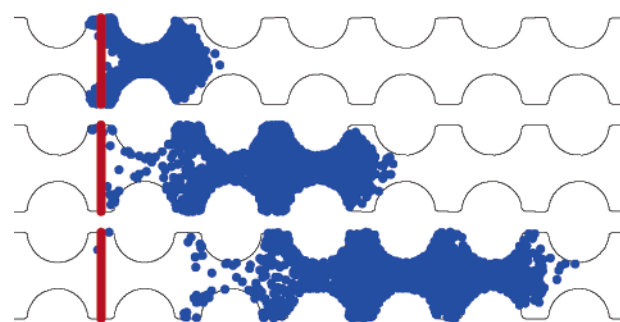


Figure 4. Time series of solute transport in an in-line circle post array ($m = 0.35$, $Pe = 100$, $N = 2000$). The lines on the left of each figure show the initial positions of the particles. The frames correspond to $t = 0.1, 0.3$, and 0.5 .

227 This method was validated against theory for pressure-driven
 228 flow between flat plates¹³ using various values of N . Excellent
 229 agreement, achieving goodness of fit of $\chi^2 = 0.19$ was obtained
 230 nearly independently of the choice for $N > 5000$. For the
 231 simulations presented here, $N = 50\,000$ just to keep statistical
 232 error as low as reasonable. This approach still has a much lower
 233 computational cost than finite differences or elements when
 234 $Pe > (N/10)^{2/3} = 300$. We wish to perform high Pe simulations to
 235 reveal asymptotic behavior, so this approach offers significant
 236 savings.

237 Figure 3 shows the flow field solution (potential lines and
 238 streamlines) as well as early time evolution of the scalar field.
 239 The figure shows the transport of particles with diffusion com-
 240 pletely turned off ($Pe = \infty$) as well as $Pe = 100$ cases for a
 241 sinusoidal wavy channel. Figure 4 shows similar results for a
 242 periodic array of circular posts. For each individual geometry,
 243 simulations were performed at values of Pe from 10^{-1} to $10^{3.5}$
 244 at half-decade intervals in order to obtain information in practical
 245 ranges of Pe as well as to gain insight into asymptotic behavior at
 246 large Pe .

247 The simulations are run for a much longer time than is shown
 248 in Figures 3 and 4. They are typically run so that the solute band
 249 runs at least $Pe/2$ channel widths downstream or until the
 250 bandwidth σ is at least 10 channel widths in axial extent. We also

require convergence to “late time” behavior. This is determined
 by monitoring the variance (σ^2) of the particle locations in the
 axial direction, and the error on the variance³⁵ $\sigma_\sigma^2 = \sigma^2(2/N)^{1/2}$,
 at every time step of the simulation. Convergence in the slope of
 $\sigma^2(t)$ is judged to be achieved when the slopes change by less
 than 0.5% when the number of time steps is doubled. Dispersion
 coefficient is then calculated as $D_L = \sigma^2/2t$; estimated error on
 this quantity based on the convergence criterion is 1%.

RESULTS

Dispersion Coefficients. The key results of this paper are
 the normalized dispersion coefficients D_L/D_{12} for the post arrays
 (Figure 5) and wavy channel geometries (Figure 6). In each plot,
 the dispersion for pressure-driven flow through a uniform 2D
 channel¹³ is also plotted for comparison. Not surprisingly, signifi-
 cantly higher dispersion is found at larger m . At large Pe , we note
 that the effective diffusivity appears in all cases to be asymptotically
 approaching proportionality to Pe^2 . For a given post size m , we
 also observe that diamond shapes confer the smallest dispersion
 of the three geometries, and squares confer the most dispersion.
 Interestingly, the plot for square posts shows that, at high fill
 factors, electrokinetic flow through square post arrays can create
 even more dispersion than pressure-driven flow through straight
 channels. Of course, this is not entirely a fair comparison from a
 chromatographic sense, since the surface area in the latter case
 is much higher. But it does suggest that the design in Figure 1E,
 for example, may be a particularly bad choice from a good
 chromatographic resolution standpoint, while the diamond shapes
 in A–D would probably perform quite well (indeed, our results
 suggest that He et al.¹ intuitively chose a very good geometry for
 their experimental device). For wavy channels, we observe the
 somewhat surprising result that sinusoidal walls actually confer
 slightly more dispersion than sawtooth-shaped walls. At low Pe ,
 all of these partially obstructed geometries actually lead to less
 axial diffusion than would be obtained from a straight tube.

Surprisingly, out-of-phase channels result in only somewhat
 higher dispersion compared to in-phase capillary geometries. In
 contrast, Eidsath et al.¹⁹ found for pressure-driven flow that in-
 line arrays are the highest dispersion geometrical configuration
 for a given interstitial volume when compared to both staggered

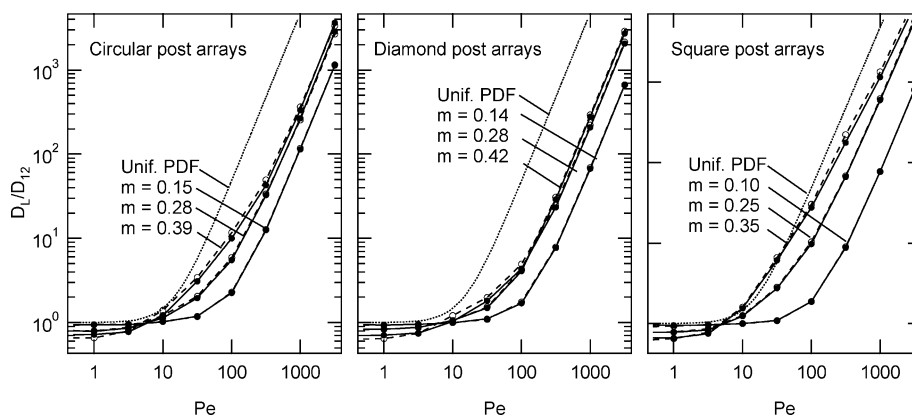


Figure 5. Effective longitudinal diffusion coefficient for post arrays of various geometries (from left to right: circles, diamonds, and squares) and amplitude denoted within each plot. In-line geometries are shown with dashed lines, staggered geometries are shown with solid lines. The fine dotted line shows effective diffusivity for pressure-driven flow through a uniform 2D channel without posts,¹³ $D_L/D_{12} = 1 + Pe^2/210$.

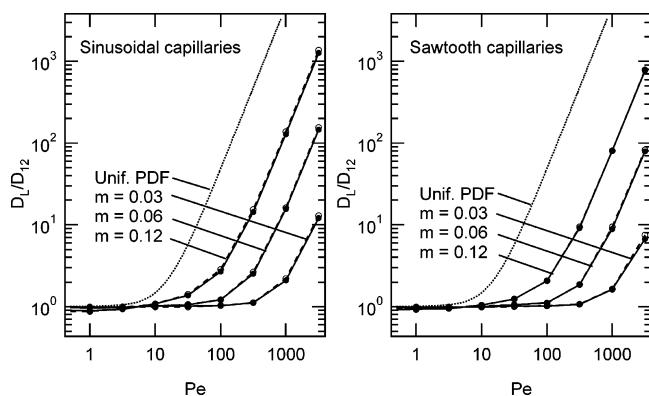


Figure 6. Effective longitudinal diffusion coefficient for wavy channels with sinusoidal (left) and sawtooth (right) wall shapes. Amplitude is denoted within each plot. In-phase walls are shown with solid lines, and out-of-phase walls are shown with dashed lines. The fine dotted line shows effective diffusivity for pressure-driven flow through a uniform 2D channel,¹³ $D_L/D_{12} = 1 + Pe^2/210$.

290 and random arrays. However, in pressure-driven flows, cavity flows
 291 with closed streamlines can form that are most pronounced in
 292 in-line geometries, and these contribute substantial dispersion.
 293 For potential flow resulting from ideal electrokinetic transport,
 294 smooth streamlines are guaranteed, and we would suggest that
 295 this character explains why the in-line and staggered arrays are
 296 not substantially different. Another reason may be our definition
 297 of Pe based on $\Delta\phi/L^*$ rather than on average flow speed. While
 298 it makes sense to base Pe on $\Delta\phi/L^*$ for an electrically driven
 299 system, the flow rate for in-line geometries is often lower than
 300 for staggered geometries at the same $\Delta\phi/L^*$. Were Pe based on
 301 average flow speed, the in-line curves would be shifted slightly to
 302 the left in these plots.

303 **Collapsing Results for All Geometries.** These figures show
 304 in nearly all cases that $D_L \propto Pe^2$ as $Pe \rightarrow \infty$. This suggested to us
 305 that there might be some hope of developing a quasi-“universal”
 306 correlation for D_L that could collapse the data from all geometries.
 307 To this end, we first normalize the dispersion coefficient D_L by
 308 its value at $Pe = 0$, which we call D_{L0} . Note that this is different
 309 from the molecular diffusion coefficient D_{12} , because of the
 310 geometric obstructions to diffusion presented by the solid bound-
 311 aries. We call this the “effective axial diffusion coefficient”.

312 Leaving aside for the moment the question of how to predict
 313 D_{L0} , we then considered what form of analytical fitting function is
 314 appropriate for D_L/D_{12} . Three fitting functions were considered.
 315 The first of these is suggested by Aris' result for a unidirectional
 316 flow:

$$D_L/D_{L0} = 1 + Pe^2/\alpha_1 \quad (3)$$

317 As discussed previously, this form was derived by Aris presuming
 318 the flow is purely axial. However, as will be shown shortly, as m
 319 increases and flow becomes less unidirectional, the relative error
 320 in such fits becomes quite large.

321 A second fit function has been suggested by the porous media
 322 community to deal with highly nonunidirectional flows:^{18,19,36,20}

$$D_L/D_{L0} = 1 + Pe^{n_2}/\alpha_2 \quad (4)$$

323 Data in the porous media literature suggest that $n_2 \approx 2$ but falls
 324 as the flow becomes more tortuous. Since this approach has two
 325 free parameters, whereas the first fit function has only one, better
 326 matching with experimental/numerical data is expected. However,
 327 the present data in Figures 5 and 6 clearly show $D_L \propto Pe^2$ at large
 328 Pe . For this reason we considered a third correlation form, which
 329 to our knowledge has not appeared in the literature previously:

$$D_L/D_{L0} = 1 + Pe/\alpha_{3,1} + Pe^2/\alpha_{3,2} \quad (5)$$

330 This form was inspired by Adler's¹⁵ suggestion that $D_L/D_{L0} \propto Pe$
 331 when dispersion is dominated by velocity variations, plus our data
 332 clearly showing that $D_L \propto Pe^2$ as $Pe \rightarrow \infty$ in Figure 7. In other
 333 words, we considered that Adler's suggestion might apply to an
 334 intermediate range of Pe . We note that, like the second fitting
 335 function (eq 4), this form has two fitting parameters; however, it
 336 has the obvious advantage that it behaves correctly at high Pe .

337 To compare these various fitting approaches, for each geom-
 338 etry (fixed shape and m), the numerical data for D_L/D_{L0} versus
 339 Pe were fit by these three functions, using the method of

(36) Probstein, R. F. *Physicochemical Hydrodynamics*, 2nd ed.; Wiley: New York, 1994.

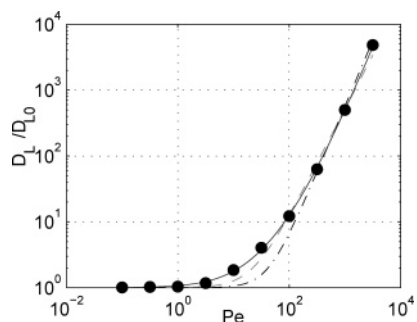


Figure 7. Best-fit curves for in-line circle post array dispersion results at $m = 0.35$. Values for free parameters can be found in Table 1. The first, second, and third fit functions are denoted by the dash-dot, dash, and solid curves, respectively.

Table 1. Fit Parameters and Length Scales for In-Line Circles

m	D_{L0}	$\alpha_1^{1/2}$	χ^2_1	$\sqrt[2]{\alpha_2}$	n_2	χ^2_2	$\alpha_{3,1}$	$\alpha_{3,2}^{1/2}$	χ^2_3
0.150	0.922	88	21	84	1.955	16	286	91	6
0.169	0.906	75	32	71	1.947	24	191	78	8
0.200	0.883	62	52	56	1.928	37	112	65	9
0.226	0.862	55	76	49	1.912	53	78	58	11
0.250	0.843	50	118	43	1.892	83	54	54	16
0.282	0.794	45	213	36	1.847	144	32	49	26
0.300	0.774	44	266	33	1.808	163	26	48	22
0.339	0.726	42	458	25	1.692	229	16	48	18
0.350	0.703	42	527	22	1.640	227	14	48	13
0.357	0.690	42	586	21	1.606	244	12	49	12
0.395	0.657	44	865	14	1.454	178	9	52	25

340 maximum likelihood³⁷ (minimum χ^2 , where χ^2 is the goodness of
 341 fit). Each different geometry had a different set of fit coefficients,
 342 but correlating the results with the parabolic function (eq 5)
 343 consistently achieved much smaller χ^2 than the other fitting
 344 functions. Figure 7 shows an example of this for the circular post
 345 data at $m = 0.35$. Previously suggested correlation functions have
 346 significant error near Pe 10–100. Only the parabolic form (eq 5),
 347 suggestive of an asymptotic series, performs well at all Pe and
 348 large feature amplitude m .

349 This is shown in more detail in tabular form for all circular
 350 post geometries in Table 1: curve fit coefficients as well as χ^2
 351 goodness-of-fit parameters χ^2_1 , χ^2_2 , and χ^2_3 (corresponding to the
 352 three curve fits, eqs 3–5, respectively) are given for the case of
 353 circular posts. Additional data for other geometries are reported
 354 in Supporting Information. As clearly shown in the tables, the χ^2
 355 values for the new correlation function (last column of Table 1)
 356 are dramatically lower at high values of m .

357 Now having identified eq 5 as the best form for fitting the data,
 358 the task remains to find a “universal” means for predicting the
 359 correlation coefficients α for different geometries and various m .
 360 To account for the fact that diamonds and circles, for example,
 361 have different dispersion coefficients at the same m , we turn to
 362 Johnson et al.,^{38,39} who suggested an effective pore size Λ^* for
 363 porous media to serve as a means for normalizing Darcy
 364 permeabilities of different pore geometries:

(37) Bevington, P. R.; Robinson, D. K. *Data Reduction and Error Analysis for the Physical Sciences*, 2nd ed.; McGraw-Hill: New York, 1992.

(38) Johnson, D. L.; Koplik, J.; Schwarz, L. M. *Phys. Rev. Lett.* **1986**, *57*, 2564–2567.

(39) Johnson, D. L.; Loplik, J.; Dashen, R. J. *Fluid Mech.* **1987**, *176*, 379–402.

$$\Lambda^* \equiv \frac{2 \int_A |\mathbf{u}|^2 dA}{\int_p |\mathbf{u}|^2 dp} \quad (6)$$

365 where p is the wetted perimeter per unit length of the periodic
 366 domain, \mathbf{u} is the velocity (assuming potential flow), and A is the
 367 cross-sectional area. In the case of straight tubes of arbitrary cross-
 368 section geometry, this is equivalent to half the hydraulic diameter
 369 $d_h = 4A/p$ since the velocity is uniform for straight tubes in
 370 potential flow. In keeping with other length scale normalizations
 371 throughout this paper, we normalize $\Lambda = \Lambda^*/L^*$. As an aside,
 372 the Johnson et al. formulation also has a parameter they called
 373 the “formation factor”, F , which relates to the effective open area
 374 of the medium. The length scale Λ and $1/F$ are similar to the
 375 tortuosity and porosity (respectively) more often used to describe
 376 porous media. For axially varying geometries, the value of Λ must
 377 be calculated using a potential flow solver in general. We tabulate
 378 Λ for each geometry and m in the Supporting Information, but it
 379 can also be easily estimated for slowly varying geometries in the
 380 lubrication theory limit. That is, if $A(x)$ does not vary too quickly,
 381 one can assume that \mathbf{u} is nearly uniform across the cross section,
 382 and from continuity $u(x) \approx Q/A(x)$. Given an axial profile $A(x)$,
 383 the above integral can be evaluated directly. The simplified form
 384 on the right-hand side comes from using relations developed
 385 above and the definition of the Jacobian to scale differential
 386 volumes between variable spaces ($dx dy = J d\phi d\psi$).

387 This normalized effective pore size $\Lambda = \Lambda^*/L^*$ collapses much
 388 of the numerical data we have obtained to a nearly “universal”
 389 dispersion law for the geometries studied. For starters, in the case
 390 of pure diffusion ($Pe = 0$), all data from all geometries studied
 391 are reasonably well correlated by $D_{L0}/D_{L2} = \Lambda^{0.32}$ as shown in
 392 Figure 8. We have also found a minimum χ^2 correlation for all
 393 available numerical data as follows:

$$\frac{D_L}{D_{L2}} = \Lambda^{0.32} \left[1 + \frac{Pe}{7.01(1-\Lambda)^{-3.04}} + \frac{Pe^2}{343.3(1-\Lambda)^{-3.02}} \right] \quad (7)$$

394 which predicts all simulated effective longitudinal diffusivities
 395 within a factor of ~ 2 for $\sim 95\%$ of the cases simulated, and within
 396 a factor of 3 for all cases simulated. For increased accuracy,
 397 however, one might prefer to use the geometry-specific correla-
 398 tions given in Table 2. Geometry-specific correlations predict
 399 longitudinal effective diffusion coefficients to within a factor of
 400 2.2 of all numerical data at all Pe .

401 We note that free best-fit parameters found in eq 7 seem close
 402 to round numbers, suggesting a power-series expansion. That is,
 403 that the expression could have been written almost to within three
 404 significant digits of accuracy as

$$\frac{D_L}{D_{L2}} = \Lambda^{1/3} \left[1 + \frac{Pe}{7(1-\Lambda)^{-3}} + \frac{Pe^2}{7^3(1-\Lambda)^{-3}} \right] \quad (8)$$

405 While this is an interesting note, we believe this to be purely
 406 fortuitous, although the simplified dependencies on Λ that can
 407 be derived may be easier to remember as rules of thumb.

408 **Comparison with Pure Diffusion and Pressure-Driven**
 409 **Flow.** We take a moment to compare the dispersion from pure

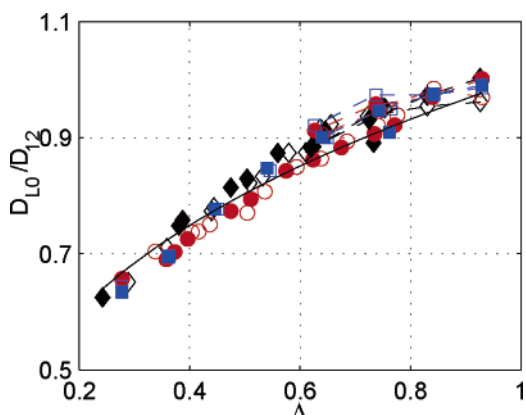


Figure 8. Apparent axial diffusion coefficient at $Pe = 0$ (pure diffusion). Post arrays are represented by points *not* connected by dashed lines, and each marker symbol (diamonds, circles, squares) correspond to the post shape. Points representing in-line and in-phase geometries are filled in. Sinusoidal channels are represented by diamonds. Parameters for capillary geometries are connected by dashed lines to guide the eye in distinguishing them from post array cases. The solid line shows $D_{L0}/D_{12} = \Lambda^{0.32}$

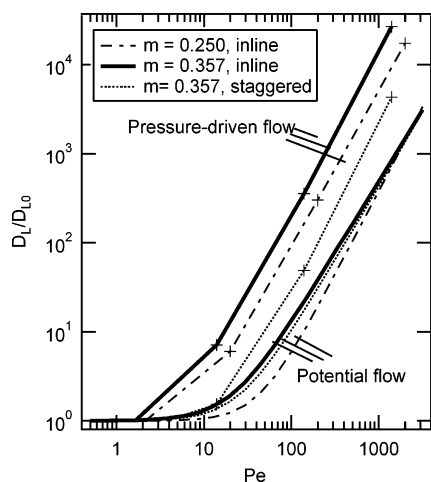


Figure 9. Dispersion coefficient at various Pe due to pressure-driven flow, compared with pure electrokinetic flow through circular post arrays. Computational results for pressure-driven flow are from Edwards et al.,¹⁸ shown as lines connecting their data points (+ symbols) to guide the eye.

Table 2: Correlations Used To Predict Dispersion According to Eq 5

geometry	D_{L0}/D_{12}	$\alpha_{3,1}$	$\alpha_{3,2}^{1/2}$
diamonds	$\Lambda^{0.30}$	$8.17(1 - \Lambda)^{-3.21}$	$38.21(1 - \Lambda)^{-0.71}$
circles	$\Lambda^{0.34}$	$3.98(1 - \Lambda)^{-2.97}$	$36.50(1 - \Lambda)^{-0.55}$
squares	$\Lambda^{0.33}$	$2.23(1 - \Lambda)^{-3.82}$	$19.61(1 - \Lambda)^{-1.16}$
sinusoidal	$\Lambda^{0.24}$	$6.97(1 - \Lambda)^{-2.90}$	$19.53(1 - \Lambda)^{-1.50}$
sawtooth (BT)	$\Lambda^{0.19}$	$8.66(1 - \Lambda)^{-3.09}$	$24.57(1 - \Lambda)^{-1.47}$
sawtooth (SC)	$\Lambda^{0.18}$	$14.02(1 - \Lambda)^{-2.77}$	$24.58(1 - \Lambda)^{-1.49}$

410 electrokinetic flow with previous work on pressure-driven flow in
 411 similar geometries. Edwards et al.¹⁸ gave values for longitudinal
 412 dispersion in the limit of pure diffusion ($Pe = 0$) for two in-line
 413 circular post arrays and staggered circular post arrays. The current
 414 results are in agreement to within 4% of their results.

415 Edwards et al. also calculated values for longitudinal dispersion
 416 due to pressure-driven flow at various values of Pe . Noting that
 417 they defined Pe slightly differently, selected data for three

representative cases from Edwards et al.¹⁸ are compared with fits 418
 to our electrokinetically driven circular post cases in Figure 9. 419
 Dispersion is significantly higher in the pressure-driven flow 420
 case—as much as an order of magnitude higher depending on 421
 the case and the Peclet number. Interestingly enough, for 422
 pressure-driven flow, the staggered array ($m = 0.357$) is far less 423
 dispersive than either of the in-line cases. The effect of staggered 424
 versus inline is not nearly so pronounced for electrokinetic flow. 425

We also note that Blom et al.⁴⁰ performed simulations and 426
 experiments to measure dispersion in a variety of square post 427
 array and sawtooth capillary geometries under electrokinetic flow. 428
 Values of Λ calculated from the velocity field and used to calculate 429
 α_1 according to correlations similar to those in Table 2. Observations 430
 indicate that results for the square post array agree within 431
 a factor of 2. 432

CONCLUSIONS

This paper presents computations of effective longitudinal 433
 diffusion due to geometric dispersion in pure electrophoretic 434
 (potential) flow around post arrays and wavy-walled channels. It 435
 is hoped that these results provide useful engineering rules for 436
 column designs in electrokinetically driven chromatography systems, 437
 as well as systems with mixed electrokinetic and pressure- 438
 driven flow, by using previously reported results.¹⁸ Thus, the data 439
 are presented in a practical format in Figures 5 and 6. Additionally, 440
 a quasi-“universal” correlation for (eq 7) should predict D_L to 441
 within a factor of 3 (and therefore predict bandwidths to within a 442
 factor of $3^{1/2}$) for geometries similar to those studied here. In 443
 general, at high Pe the results show that $D_L \propto Pe^2$ for all 444
 geometries as $Pe \rightarrow \infty$. 445
 446

Dispersion from square posts is the highest for the geometries 447
 studied and from diamonds the least. In the case of relatively large 448
 in-line squares, the dispersion in electrophoresis is nearly as high 449
 as in pressure-driven flow, owing to the large path length 450
 differences from streamline to streamline in the domain. At 451
 relatively high Peclet numbers (say 100) and for relatively large 452
 diameter posts, the square posts give effective an effective 453
 diffusivity D_1/D_{12} that is ~ 3 times that for circular posts (keeping 454
 diameter of circular post equal to the side length of the square 455
 post). Diamond posts give effective diffusivities that are still 456
 another factor of 2 lower than for circular posts. Keeping Peclet 457
 number below 30 and using diamond-shaped posts should ensure 458
 that geometric band broadening is never more than 40% more 459
 than broadening due to binary diffusion in a straight channel. The 460
 results for wavy-walled channels show that if the roughness is 461
 less than $\sim 5\%$ of the total width of the channel, the additional 462
 dispersion can be kept to less than 40% of that due to binary 463
 diffusion as long as $Pe < 200$. 464

The numerical results presented in this paper only describe 465
 the fully developed late-time dispersion. In future work, we plan 466
 to analyze early-time behavior as well in order to characterize the 467
 performance of relatively short columns. 468

SUPPORTING INFORMATION AVAILABLE

Additional information as noted in text. This material is 469
 available free of charge via the Internet at <http://pubs.acs.org>. 470
 471

Received for review July 2, 2004. Accepted December 2, 472
 2004. 473

AC049022K 474

(40) Blom, M. T.; Hasselbrink, E. F.; Wensink, H.; van den Berg, A. *Micro Total Analysis Systems 2001*; Monterey, CA, 2001.